Misan Journal of Engineering Sciences ISSN: 2957-4250
Vol. 5, No. 1, 28 June 2026. ISSN-E: 2957-4242

In-situ synthesis of Medium-Entropy $(HfZrTi)B_2$ Ceramic Composite from Initial Oxide Powders

Ekhlas Q. Khalaf[1], Zohre Balak[2]*
Department of Materials Science and Engineering,
Islamic Azad University, Iran[1]
** Corresponding author E-mail: Engakqays009@gmail.com*

(Received 11 March, Revised 28 April, Accepted 4 May)

Abstract
In the current work, the B_2 medium-entropy, ceramic composite $(HfZrTi)B_2$ was in situ synthesized through reactive spark plasma sintering (RSPS) at 2000 °C and at two loadings of B_4C powder, 10 minutes. The obtained specimens were described based on the microstructure, relative density, hardness, and fracture toughness. The data show that the increase in the B_4C content significantly enhances the reduction reaction of the oxide precursors, therefore, leading to the formation of the $(HfZrTi)B_2$ phase to a higher degree. The lattice-parameter calculations provided a value of 14.7668 A of the stoichiometric composition and a value of 3.14985 A of the sample with the increased B_4C content, which has validated the insertion of a larger lattice distortion in the sample with the higher B_4C content. Additionally, the specimen with higher B_4C also obtained a lower porosity of 12.9% and a hardness value of 10.6 Gpa, as compared to the other specimen with lower B_4C loading, which had a porosity of 17.7% and a hardness of 9.4 Gpa. The fracture toughness could not be measured due to relatively high porosity.

Keywords: Fracture toughness; Hardness; ultra-high-temperature ceramics; reactive spark plasma sintering; $(HfZrTi)B_2$; sinterability

1. Introduction

It has already been established that refractory ceramic compounds such as carbides, borides, and nitrides possess very high melting points, high hardness, chemical inertness, and strong oxidation resistance. These characteristics have made them attractive subjects in terms of application in extreme conditions and thus, resulted in the labeling of them as ultra-high temperature ceramics (UHTCs). Among these materials, transition-metal diborides exhibit particularly favorable oxidation resistance compared with other refractory intermetallics. Hafnium diboride (HfB_2) and zirconium diboride (ZrB_2) have therefore been widely recognized as leading materials for high-temperature aerospace components, including missile nose cones, sharp leading edges, turbine blades, and structures used in high-speed or next-generation aircraft [1–5]. Titanium diboride (TiB_2), owing to its high strength, low density, excellent wear and corrosion resistance, and very high hardness arising from strong covalent B–B bonding, has also been found in extensive industrial applications [6].

DOI: https://doi.org/10.61263/mjes.v5i1.283
This work is licensed under a Creative Commons Attribution 4.0 International License.

In recent years, UHTCs based on solid-solution carbides, diborides, and silicides of transition metals have emerged as a new class of advanced refractory materials. Following the conceptual developments in metallurgy, these ceramics are categorized as medium-entropy (three to four principal components) and high-entropy (five or more components) systems. Several studies have demonstrated that medium-entropy ultra-high-temperature carbides and borides can significantly enhance physical and mechanical properties due to their unique lattice-distortion effects [7–10].

In both solid-state and liquid-phase syntheses, high-entropy carbides have been produced with the use of powders (as seen in [11-13]). Zhou et al. [11] demonstrated the synthesis of C (Ti 0.2 Zr 0.2 Nb 0.2 Ta 0.2 Hf 0.2) powders through the reactive spark plasma sintering (RSPS) method and they obtained particle sizes of approximately 2μm at 1950 °C. The same composition was also prepared by Moskalykh et al. [12] through reactive high-energy ball milling of metallic powders, and graphite, but impurities like oxygen and iron could be easily introduced in the process. Liu et al. [13] prepared the high-entropy carbide C(Mo 0.25Nb 0.25Ta 0.25W 0.25) by direct reaction of metallic powders with graphite at 1800 °C , nevertheless, but the resulting particle size remained relatively coarse (≈9 μm).. Also, C (Ti 0.25Zr 0.25Nb 0.25Ta 0.25) was synthesized by other researchers [11] through a one-step carbothermal reduction of oxide powders by graphite at 2200 °C producing particles of sizes ranging between 0.5 to 2 μm.

The study of Lichen et al. [9] combined both the theoretical modelling and the experimental observation to determine the lattice parameters, mechanical properties, electronic density, and charge density distribution of the medium-entropy carbides (MoTaW) C and (NbTaW) C. Their results indicate that the mechanical performance of medium-entropy carbides is significantly higher when in comparison with the performance of high-entropy alloys, and this is largely due to the strong lattice distortion caused by the interstitial carbon atoms. This deformation facilitates charge movement among metallic cations and non-metallic anions thus increasing covalent bonding as well as mechanical properties.

More recently, the medium-entropy carbide (TiZrHf)C with high strength has been synthesized, and its structure was shown to remain stable under pressures ranging from 0 to 100 GPa. Random elemental distribution and atomic-size mismatch generate localized lattice distortions. Increasing pressure further amplifies these distortions, while also elevating the elastic moduli, anisotropy, sound velocity, and Debye temperature [8]. In another study, (TiZrHf)C ceramics fabricated by hot pressing achieved a relative density of 99.2%, an average grain size of 1.9 ± 0.6 μm, a room-temperature flexural strength of 579 ± 62 MPa, and a flexural strength of 619 ± 57 MPa at 1600 °C, outperforming their single-component counterparts TiC, HfC, and ZrC [10]. Medium-entropy (TaTiZr)C ceramics synthesized via spark plasma sintering at 1973 °C exhibited a flexural strength of 700 MPa and a fracture toughness of 3.2 MPa·m^0.5 at room temperature, while heating to 1800 °C caused decomposition of the single-phase structure and increased the fracture toughness to 4.4 MPa·m^0.5 [7].

Given the growing interest in entropy-stabilized UHTCs and the need for improved high-temperature performance, the present work focuses on the in-situ synthesis of a boride-based ceramic composite using oxide precursor powders. The microstructure, porosity

(open and close), hardness and fracture toughness of the fabricated composite are systematically evaluated to provide insights into its potential for high-temperature structural applications. It should be noted that the wear resistance is not measured in this study due to the lower hardness of fabricated samples and lack of importance.

2. Experimental Procedure

The starting materials used in this study included ZrO_2, TiO_2, HfO_2, B_4C, and nano-sized carbon black (C.Bn). The particle size, purity, and manufacturers of the raw powders are listed in Table 1. To achieve the in-situ synthesis of the $(HfZrTi)B_2$ composite, oxide precursor powders were mixed with the reducing agents B_4C and nano-sized carbon black (Table 1). For the first composition, the powders were weighed according to the stoichiometric ratios required for the formation of the target phase. For the second composition, the amount of B_4C was increased by a factor of 1.1 relative to the stoichiometric requirement.

The synthesis was carried out using reactive spark plasma sintering (RSPS). The processing parameters were fixed at a temperature of 2000 °C, a holding time of 10 min, and an applied uniaxial pressure of 35 MPa.

Table 1. Raw materials used in this study along with their specifications.

Powder	Particle Size	Company
ZrO_2	5 µm	Afagh Refractory, Manufactoring UHT Ceramics
B4C	10 µm	Northwest Institute for Non-Ferrous Metal Research, China, 98.7% purity
HfO_2	1 µm	Pishro ceramic mehr, 99.5% purity
TiO_2	20 µm	Alfa company
Nano carbon black	50 nm	US Research Nanomaterials, Inc; C > 95%,

For powder mixing and mechanical activation, a SPEX mill operating at 7000 rpm was employed. Prior to milling, the SPEX cups were filled with glass fragments and cleaned thoroughly to ensure the removal of any residual contaminants. After cleaning, the oxide

precursor mixture was placed in the milling cups along with ethanol and zirconia milling media, using a 1:5 powder-to-ball mass ratio. Milling of the blend was done in 1 hour at a rotational speed of 7000 rpm. Following milling, the resulting slurry was transferred to a beaker and placed in a magnetic stirring system with heating to 160-200 °C to enable the evaporation of any remaining ethanol. Since some agglomeration had occurred during drying, the powders were then carefully ground in an agate mortar to a fine, uniform powder suitable for use as a compact. The resulting powders were injected into graphite dies, and reactive spark plasma sintering (SPS) at 2000 °C under a pressure of 35 MPa was performed on the mix for 10 minutes. The products of the resulting consolidated specimens were discs with a diameter of 1.5 cm. To perform the microstructural analysis and mechanical testing, an electrical discharge (EDM) of wire-cut sectioning was used on the sintered discs. The Archimedes method is used to obtain sample densities. Vickers hardness were reported using a 30-kg load with a 10-s dwell time, and the reported values were based on the mean of five indentations. The hardness calculation was performed:

$$H=\frac{1.85F}{a\text{^}2}\ . \qquad (1)$$

The data on hardness of the samples was determined based on Equation (1), where F is the load which is applied and a is the average diagonal length of the indentation. More so, the fracture toughness of the specimens was determined by the crack length measurement method based on Anstis equation:

$$K_{IC}=0.016\ (\frac{E}{H})^{1/2}PC^{-1.5} \qquad (2)$$

As stated in the Eq (2) the stiffness of the materials in question is represented by the Youngs modulus (E), the load applied is defined as P, the crack length is expressed as 2 c and the hardness is expressed as H. Microstructural analyses were carried out to determine the toughness-mechanisms involved, using optical microscopy and field-emission scanning electron microscopy (FE-SEM).

3. Results and Discussion

3.1. Microstructural Analysis

The FE-SEM micrographs of sample A1 and A2 are exhibited in Figure 1. The microstructure of the two samples consists of grains which have different contrast. The bright, gray, and dark areas were HfB 2, ZrB 2, and TiB 2 in sample A1, correspondingly. This contrast differentiation can

be explained by Z -contrast in which the phases with the elements of higher atomic number are seen to be brighter in the backscattered electron imaging. Figure 1 also shows that point EDS analyses were carried out on two bright regions (points 1 and 2). Hafnium leads in the elemental

composition in both sites with weights of 34.75% and 41.25%, respectively. These results support a correlation between the bright contrast and the existence of the Hf -rich phases, as in the atomic-number contrast mechanism, presented above. Sample A2 has a microstructure with mostly a light-gray structure, indicating that the constituent phases were more homogeneously distributed compared to sample A1.

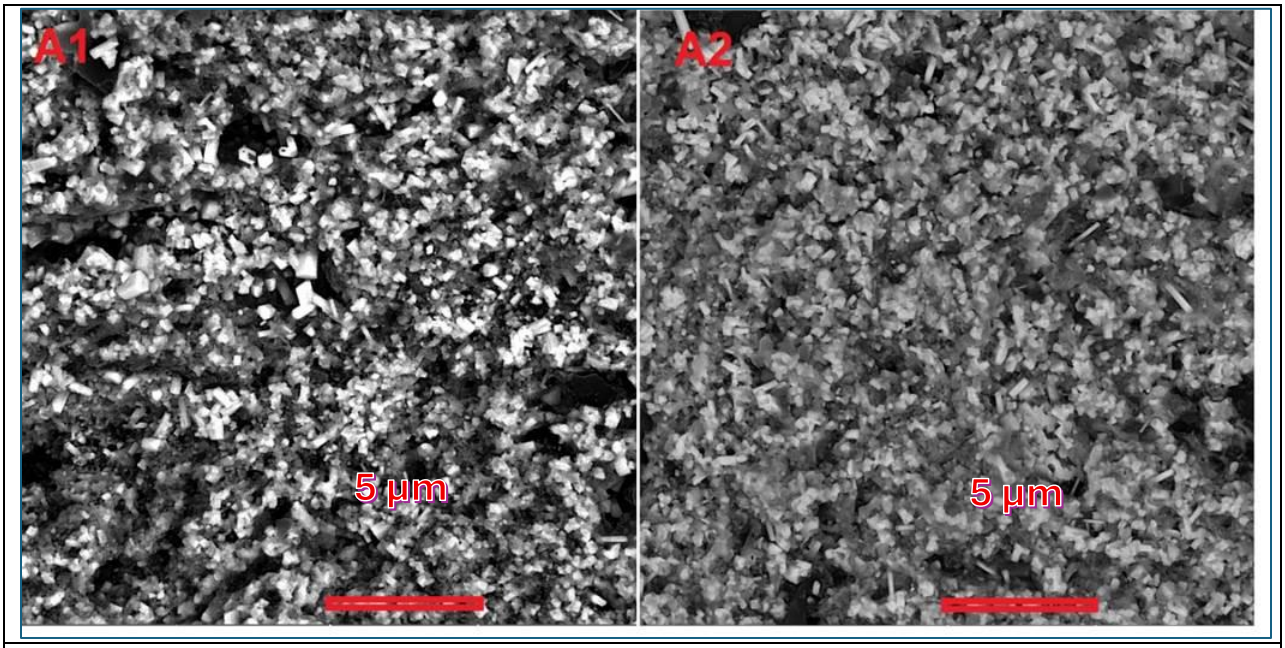


Figure 1. The FESEM images of polished surface of samples A1 and A2 as well as their point analysis.

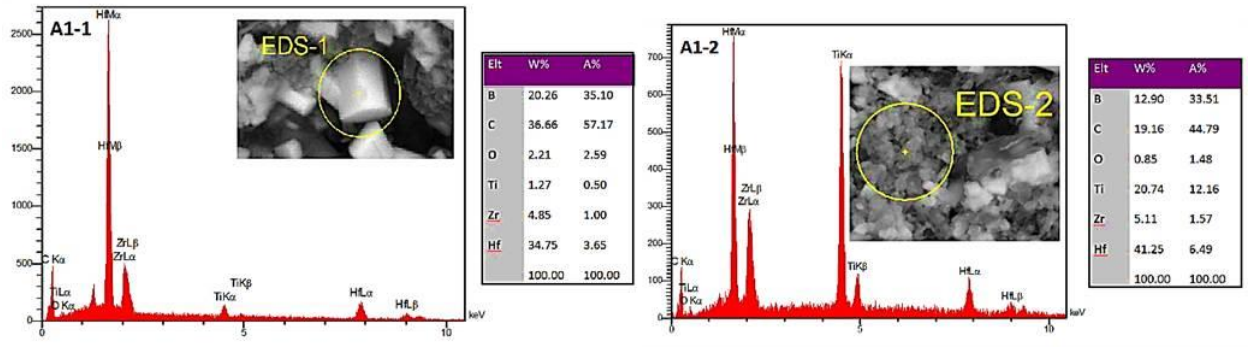


Figure 2- FESEM micrographs of samples A1 and A2

It appears that in sample A2, the HfB_2, ZrB_2, and TiB_2 phases have dissolved into one another, forming a solid solution of $(HfZrTi)B_2$, which is observed as a light-gray contrast in the FE-SEM

images. In other words, the dissolution of the bright (HfB_2), gray (ZrB_2), and dark (TiB_2) regions results in the formation of a more homogeneous light-gray solid-solution phase. This interpretation is further supported by the XRD results discussed in the following section.

Moreover, comparison of the FE-SEM micrographs of samples A1 and A2 are exhibited in Figure 2 reveals that the number of regions with distinct contrast is significantly higher in sample A1. his observation indicates that a larger fraction of the solid-solution phase has formed in sample A2, consistent with the enhanced reaction progress in the composition containing excess B_4C.

Figure 3 presents the elemental distribution map of sample A1. The elements Hf, Zr, Ti, C, and O were detected. Considering that the starting materials consisted of oxide powders (HfO_2, TiO_2, ZrO_2) along with B_4C and nano-sized carbon black (C.Bn), the small amount of oxygen detected (less than 5 wt%) indicates that the oxide phases were effectively reduced during the reaction according to Reaction (3), leading to the formation of boride phases and the release of CO gas, which escaped from the system.

$$ZrO_2+HfO_2+TiO_2+B_4C+C \leftrightarrow ZrB_2+TiB_2+HfB_2+CO_{(g)} \quad (3)$$

Thermodynamic evaluation of the reaction using HSC software indicates that it becomes feasible at approximately 1330 °C ($\Delta G_{1330} = -0.294$ kcal), confirming the spontaneity of the process. Also, according to Figure 3, a nearly uniform distribution of the constituent elements throughout the microstructure, supporting the formation of the ternary solid solution $(HfZrTi)B_2$. To further verify this, the XRD patterns of both samples which were analyzed via MAUD software are presented in Figure 4.

In sample A1, the identified phases include carbon, and the HfB_2 (or exactly ternary solid solution $(HfZrTi)B_2$). The appearance of the new $(HfZrTi)B_2$ phase, together with the absence of the initial oxide phases TiO_2, HfO_2 and ZrO_2, indicates that during sintering at 2000 °C, the oxide precursors were effectively reduced due to Reaction (3) and converted in situ into the corresponding boride phases. Furthermore, the initial amorphous carbon black (C.Bn) was consumed during the reaction, and the remaining fraction transformed into the crystalline phases.

However, according to Figure 3, oxygen element was identified during map analysis which can be attributed to little remained initial oxide phases (such TiO_2, HfO_2 and ZrO_2) in sample A1 which suggests that the in-situ synthesis reaction (Reaction 3) did not proceed to completion.

Of course, it should be noted that the reason for no identification of oxide phases through XRD patterns analyzed via MAUD can be associated to their low amount.

ISSN: 2957-4250
ISSN-E: 2957-4242

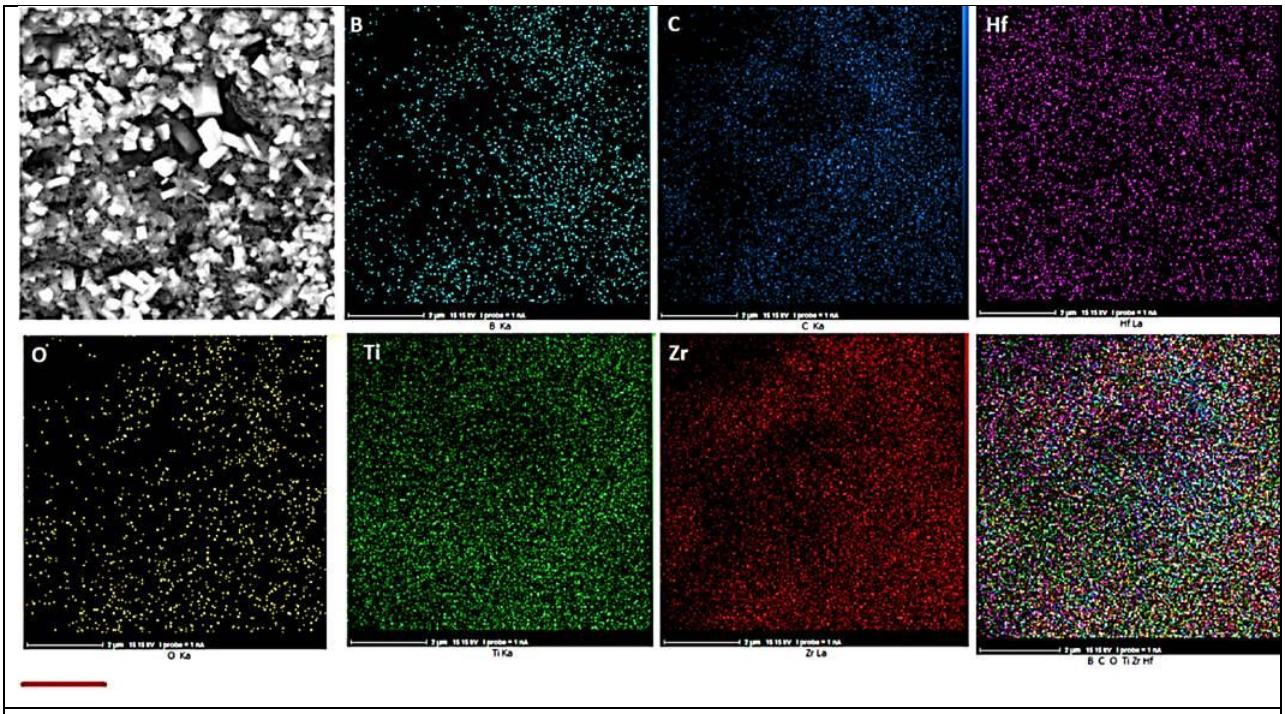
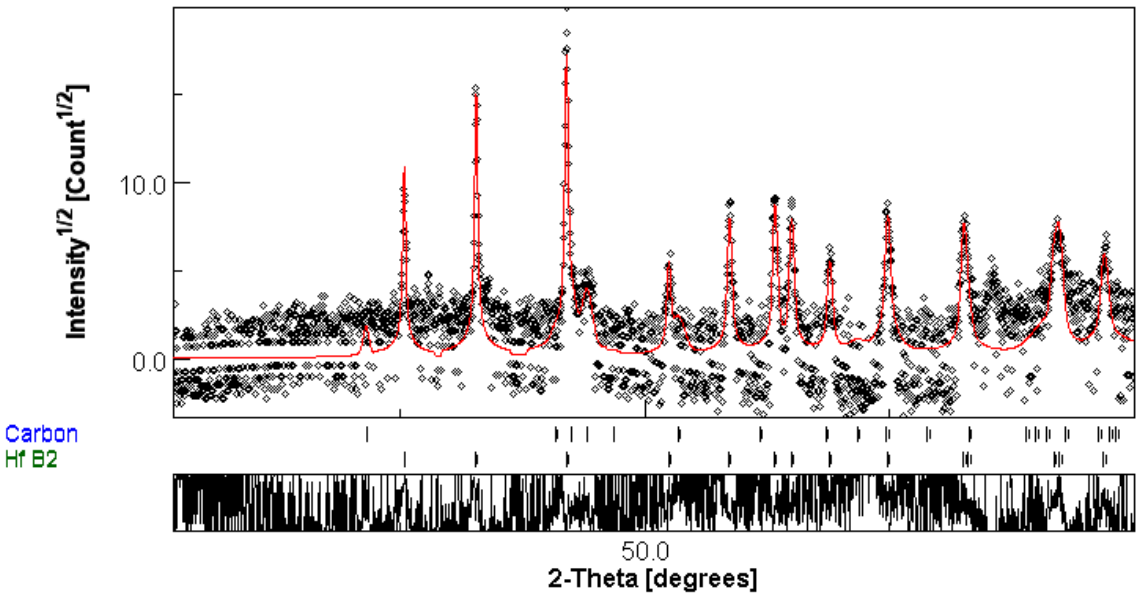


Figure 3. The elemental distribution map of sample A1

.

The XRD pattern of sample A2 which shows that has a surplus of B_4C only showed HfB_2 as seen in Figure 4, suggests an in-situ $(HfZrTi)B_2$ phase is formed. This indicates that the in-situ synthesis reaction Reaction (3) had better reaction in sample A2 than in sample A1. This finding is completely in line with the FE SEM micrographs depicted in Figure 1 as well as the elemental map analyses (seen in Figure 3). That is, the extra B_4C enabled the total reduction of the original



oxide phases and resulted in the total conversion of these phases to boride phases.

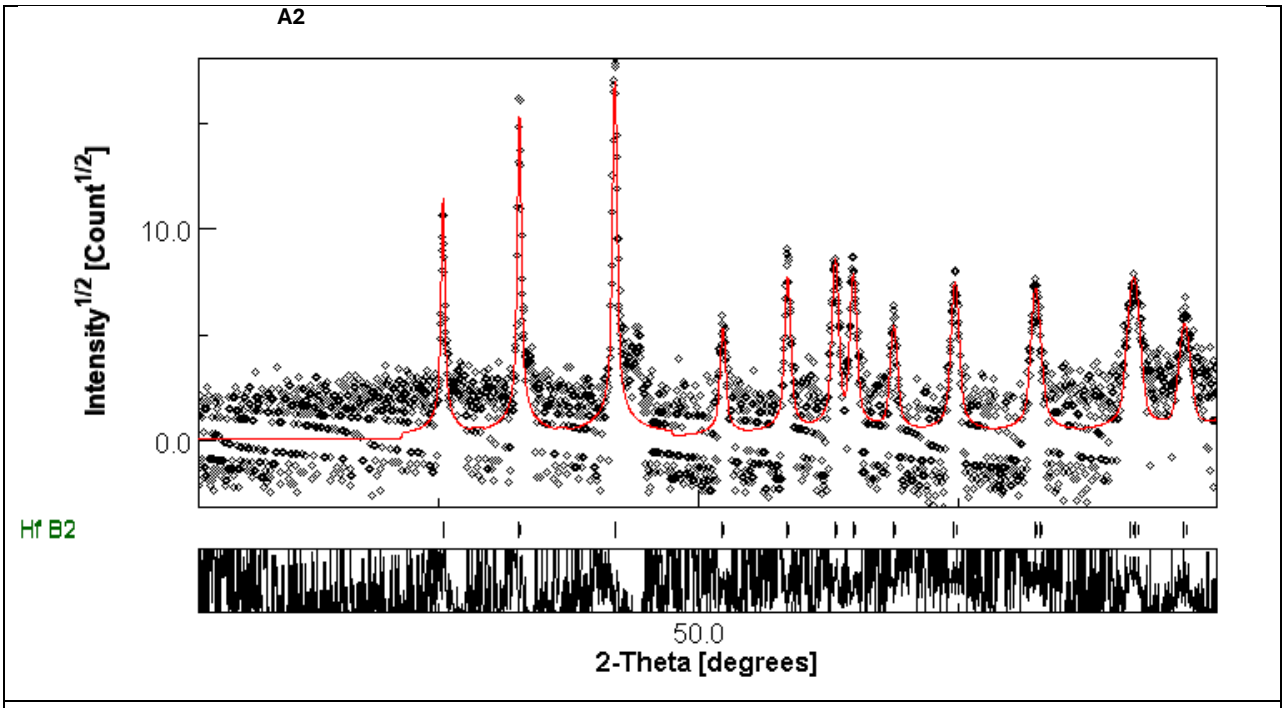


Figure 4. The XRD patterns analyzed with MAUD software.

Similar findings were reported in previous studies by Balak et al. [1, 2, 5] on ZrB_2-based ceramic composites. In those investigations, the effects of additives such as HfB_2, ZrC, and $MoSi_2$ on the microstructure of ZrB_2 ceramics were examined. A detailed microstructural examination revealed three distinct stages with white, light- gray and gray contrasts. The white phase was almost 100 percent HfB_2, whereas the light-gray phase represented (Zr, Hf)B 2 solid solution.As shown in the binary ZrB_2- HfB_2 phase diagram, the HfB_2 is fully soluble in ZrB 2 at all composition ratios to produce a continuous solid solution [13].The interplanar spacing (dspacing) was determined using X'Pert software, and the results showed values of 2.16375 Å for composite 18 and 2.16555 Å for composite 5, indicating a reduction in dspacing for composite 18 .Furthermore, the lattice parameters of ZrB_2 in composites 5 and 18 were calculated using MAUD. The results revealed that increasing the Hf content in composite 18 led to a contraction of the ZrB_2 lattice (a_5 = 3.168247 Å, c_5 = 3.530553 Å; a_{18} = 3.163609 Å, c_{18} = 3.525057 Å), confirming the dissolution of HfB_2 into ZrB_2. Due to the atomic weight of ZrC, this phase appears as a light-gray contrast in the microstructure [1–4].

The $HfZrTiB_2$ ternary solid solution formation was also confirmed by the presentation of the XRD patterns of HfB_2, ZrB_2, TiB_2 and sample A1 and A2 in Figure 5. The characteristic peaks that could be attributed to TiB_2 have completely disappeared in both samples and this means that it was dissolving into the matrix hence creating a solid solution. Also, the peaks of HfB_2 and ZrB_2 are seen to be at higher order of diffraction, an additional indication of the existence of solid solution phase.

It seems, Ti atoms, which possess smaller atomic radii compared with Hf and Zr, diffuse into the HfB_2 and ZrB_2 lattice during sintering and dissolve within its crystal structure. Consequently, the HfB_2 and ZrB_2 lattice undergoes contraction, leading to a shift of the diffraction peaks toward higher angles relative to those of their pure ones. This behavior is fully consistent with Bragg's law, according to which the interplanar spacing is inversely related to the diffraction angle. Therefore, the reduction in lattice spacing caused by lattice contraction results in an increase in diffraction angle, manifested as a rightward peak shift.

The lattice distortion results to lattice parameter changes. This change is calculated via MAUD software for HfB_2 phase. The lattice parameters of a=14.7668 Å, c=3.48676 Å and a=3.14985 Å, c=3.4919 Å were obtained for samples A1 and A2, respectively which are higher in comparison with pure HfB_2 (a=3.1425 Å, c=3.4760 Å). This issue is completely in accordance with its peak shifting as illustrated in Figure 5.

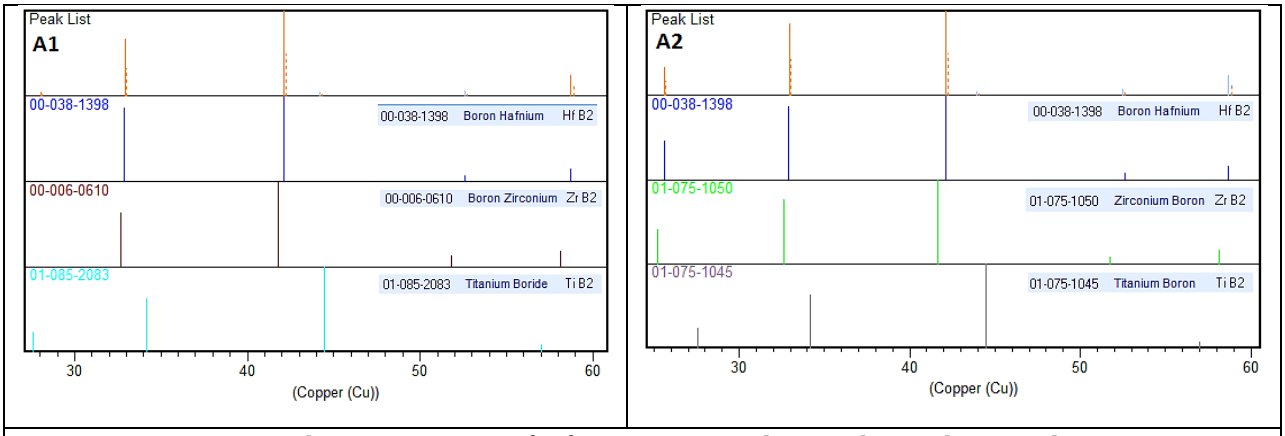


Figure 5. The XRD patterns of HfB_2, ZrB_2, TiB_2 along with sample A1 and A2.

3.2. Sinterability

Figure 6 represents the porosity of samples A1 and A2 in terms of overall open and closed porosity. As depicted by the data, sample A1 has a total porosity of 17.7% ,and sample A2 has a total porosity of 13.8%. The level of porosity in both samples is still pronounced, although a sintering temperature of 2000 0 C was used in the in-situ synthesis, which means that full densification was not attained. This is characteristic of ultra-high-temperature ceramics, which are commonly in the form of low sinterabilities due to their great melting points and the power of their covalent bonding; therefore, complete densification is achievable at high temperatures or with lengthy dwell periods.

Comparing the two samples, one can realize that A2 is not as porous as A1 is. This can be explained by the addition of excess B_4C, which both allows the in-situ reaction (Reaction 3) and a more complete conversion of the oxide precursors to boride phases, thus improving overall densification behavior.

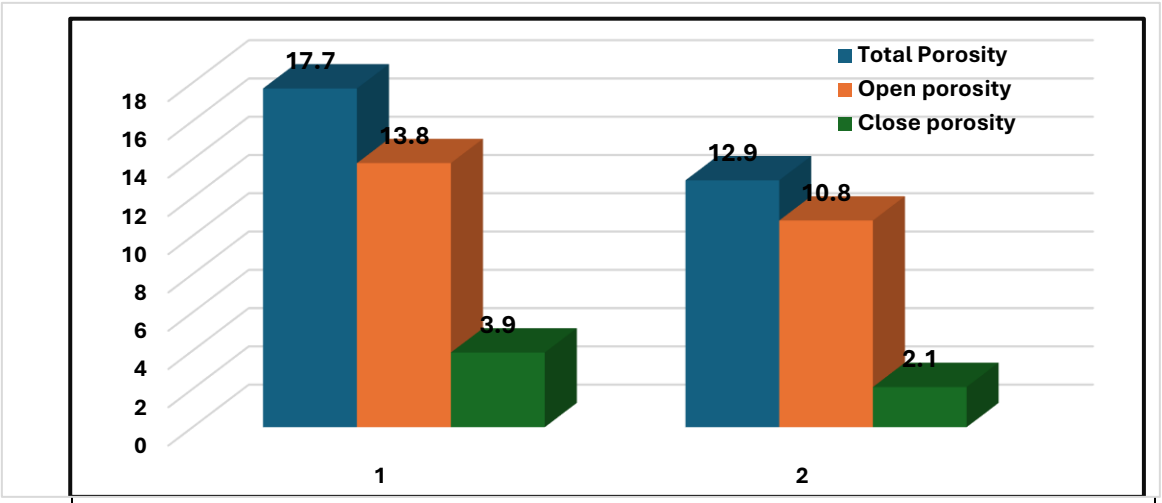


Figure 6. Total, open and close porosities of both samples

3.3. Hardness and Fracture Toughness

The hardness values of the samples were calculated by measuring the diagonal lengths of the indentations and applying the hardness equation presented in Section 3. The hardness of sample A1 was obtained as 9.4 GPa, whereas sample A2 exhibited a higher hardness of 10.6 GPa. Since hardness is strongly influenced by grain size and porosity—both of which have an inverse relationship with hardness—the lower porosity (12.9%) and finer grain size (85 nm) observed in

sample A2 account for its higher hardness in contrast sample A1 with 17.7% porosity and 100 nm grain size.

Figure 7 presents higher-magnification FE-SEM images of the indentation corners. Despite careful examination of all indentation marks, no cracks were observed in either sample. As a result, fracture toughness could not be evaluated using the crack-length method. This behavior is attributed to the relatively high porosity present in both samples, which suppresses the formation of radial cracks around the indentations. Similar observations have been reported in previous studies on graphite-reinforced ZrB_2 ceramics [14].

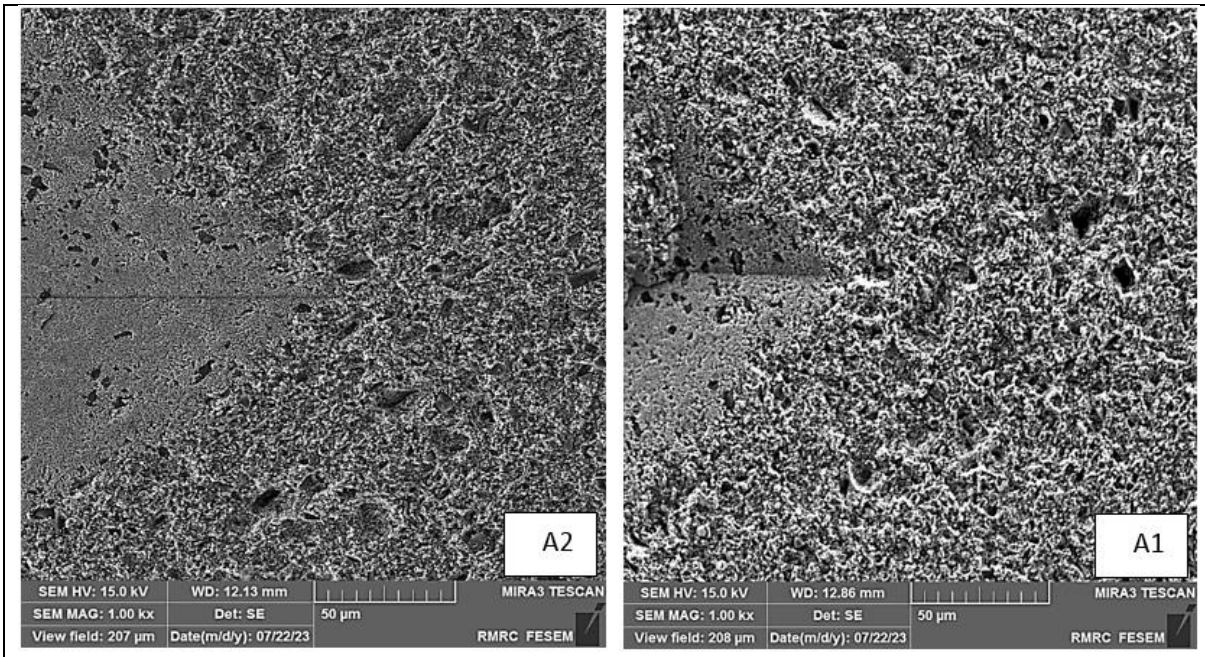


Figure 7 – High-magnification FE-SEM micrographs of the indentation corners in samples A1 and A2, illustrating the assessment of potential crack initiation around the Vickers indents.

4. Conclusions

1. The $(HfZrTi)B_2$ composite was successfully synthesized in situ from oxide precursor powders at 2000 °C with a dwell time of 10 min.
2. The presence of excess B_4C in sample A2 enhanced the reduction of the oxide powders and promoted a more complete formation of the $(HfZrTi)B_2$ phase.
3. The total porosity of samples A1 and A2 were measured as 17.7% and 12.9%, respectively, indicating improved densification in sample A2.
4. The hardness values obtained for samples A1 and A2 were 9.4 GPa and 10.6 GPa, respectively.

5. The lattice parameter for the stoichiometric composition is 14.7668 Å, while for the sample with a higher B_4C content it is 3.14985 Å, indicating a greater lattice distortion in the latter.

Author Contributions: The authors contributed to all parts of the current study.

Funding: This study received no external funding.

Conflicts of Interest: The authors declare no conflict of interest.

References

1. Balak, Z. and M. Zakeri, Application of Taguchi L32 orthogonal design to optimize flexural strength of ZrB2-based composites prepared by spark plasma sintering. International Journal of Refractory Metals and Hard Materials, 2016. **55**: p. 58-67.

2. Balak ,Z., et al., Taguchi design and hardness optimization of ZrB2-based composites reinforced with chopped carbon fiber and different additives and prepared by SPS. Journal of Alloys and Compounds, 2015. **639**: p. 617-625.

3. Balak, Z., et al., Effect of open porosity on flexural strength and hardness of ZrB2-based composites. Ceramics International, 2015. **41**.

4. Darihaki, F., Z. Balak, and R. Eatemadi, Effect of nano and micro SiC particles on the microstructure and fracture toughness of ZrB2-SiC nanocomposite produced by SPS method. Materials Research Express, 2019. **6**(9): p. 095608.

5. Kavakeb, K., Z. Balak, and H. Kafashan, Densification and flexural strength of ZrB2–30 vol% SiC with different amount of HfB2. International Journal of Refractory Metals and Hard Materials, 2019. **83**: p. 104971.

6. Akrami, S., et al., High-entropy ceramics: Review of principles, production and applications. Materials Science and Engineering: R: Reports, 2021. **146**: p. 100644.

7. Demirskyi, D., et al., High-temperature toughening in ternary medium-entropy (Ta1/3Ti1/3Zr1/3)C carbide consolidated using spark-plasma sintering. Journal of Asian Ceramic Societies, 2020. **8**(4): p. 1262-1270.

8. Jin, C., et al., A DFT insight into the mechanical, electronic and thermodynamic properties of (TiZrHf)C medium-entropy carbide ceramic. Results in Physics, 2022. **35**: p. 105341.

9. Liu, L., et al., Microstructure and mechanical properties of novel medium-entropy carbide ceramics. Computational Materials Science, 2023. **230**: p. 112464.

10. Wang, X.-F., et al., High-strength medium-entropy (Ti,Zr,Hf)C ceramics up to 1800°C. Journal of the American Ceramic Society, 2021. **104**(6): p. 2436-2441.

11. Zhou, J., et al., High-entropy carbide: A novel class of multicomponent ceramics. Ceramics International, :(17)44 .2018 p. 22014-22018.

12. Moskovskikh, D.O., et al., High-entropy (HfTaTiNbZr)C and (HfTaTiNbMo)C carbides fabricated through reactive high-energy ball milling and spark plasma sintering. Ceramics International, 2020. **46**(11, Part B): p. 19008-190.14

13. Liu, D., et al., Reaction synthesis and characterization of a new class high entropy carbide (NbTaMoW)C. Materials Science and Engineering: A, 2021. **804**: p. 140520.

14. Savari, V., Z. Balak, and V. Shahedifar, Influence of graphite platelets with and without SiC on the densification and fracture toughness of ZrB2 ceramic sintered by SPS. Carbon Letters, 2022. **32**(6): p. 1559-1566.